

# Optical properties of structurally relaxed Si/SiO<sub>2</sub> superlattices: The role of bonding at interfaces

Pierre Carrier,<sup>1</sup> Laurent J. Lewis,<sup>1,\*</sup> and M. W. C. Dharma-wardana<sup>2</sup>

<sup>1</sup>*Département de Physique et Groupe de Recherche en Physique et Technologie des Couches Minces (GCM), Université de Montréal, Case Postale 6128, Succursale Centre-Ville, Montréal, Québec H3C 3J7, Canada*

<sup>2</sup>*Institute for Microstructural Sciences, National Research Council, Ottawa K1A 0R6, Canada*

(Received 13 November 2001; published 16 April 2002)

We have constructed microscopic, structurally relaxed atomistic models of Si/SiO<sub>2</sub> superlattices. The structural distortion and oxidation-state characteristics of the interface Si atoms are examined in detail. The role played by the interface Si suboxides in raising the band gap and producing dispersionless energy bands is established. The suboxide atoms are shown to generate an abrupt interface layer about 1.60 Å thick. Band structure and optical-absorption calculations at the Fermi golden rule level are used to demonstrate that increasing confinement leads to (a) direct band gaps, (b) a blue shift in the spectrum, and (c) an enhancement of the absorption intensity in the threshold-energy region. Some aspects of this behavior appear not only in the symmetry direction associated with the superlattice axis, but also in the orthogonal plane directions. We conclude that, in contrast to Si/Ge, Si/SiO<sub>2</sub> superlattices show clear optical enhancement and a shift of the optical spectrum into the region useful for many opto-electronic applications.

DOI: 10.1103/PhysRevB.65.165339

PACS number(s): 78.66.Jg, 68.65.-k, 71.23.Cq

## I. INTRODUCTION

The initial interest in light-emitting Si-based nanostructures has led to a number of important experiments establishing that Si/SiO<sub>2</sub> superlattices (SL's) show enhanced, blueshifted luminescence.<sup>1-6</sup> While the luminescence pattern is more complex in these systems than in others, the blueshift was found to correlate with decreasing Si-layer thickness. This simple relation between the silicon-layer thickness and the luminescence peak is of great interest for applications such as Si-based light-emitting diodes (Si LED's). All reported SL energy peaks are in the lower part of the visible spectrum—the highest reported value being 2.3 eV (540 nm), i.e., green,<sup>1</sup> and the lowest 1.2 eV (1030 nm), in the near infrared region.<sup>3</sup> These SLs are really multiple Si quantum wells (MQW's), the silicon oxide layers playing the role of barriers. The thickness of the Si quantum wells,  $L_{\text{Si}}$ , is the critical parameter. A fixed  $L_{\text{Si}}$  would simply set the color of the Si-LED, while MQW's with a range of  $L_{\text{Si}}$  would span a range of colors in the luminescence.

Other systems containing confined silicon structures (besides MQW's) are, e.g., porous Si (consisting of quasi one-dimensional structures),<sup>7,8</sup> silicon nanoclusters in SiO<sub>2</sub> matrices,<sup>9</sup> nanocrystals<sup>10</sup> or dislocation loops, and quantum-dot structures made from implantation of boron<sup>11</sup> or other ions.<sup>12</sup> The choice of a particular structure, e.g., for Si-LED applications, depends on many factors: stability over time, optical efficiency at room temperature, experimental reproducibility, facility to accept *n*- or *p*-type dopants (e.g., for *n-p* junctions), ease of incorporation in ultra-large-scale-integration technology, and production costs. Si/SiO<sub>2</sub> SL's are stable structures, as opposed to porous Si. In addition, the silicon layer thicknesses in SLs are directly related to the energy peaks in the Si/SiO<sub>2</sub> luminescence spectra. This is not straightforward in porous silicon, Si clusters or nanocrystals, where pore dimensions as well as hydrogen concentrations play an uncontrolled role on the energy shift.<sup>9,13</sup>

Silicon-based structures have many advantages over structures made of other semiconductors: low cost (as compared to any of the III-V's or II-VI compounds), nontoxicity, practically unlimited availability (in contrast to germanium), and benefits from decades of experience in purification, growth, and device fabrication. However, the indirect energy gap ( $\sim 1.1$  eV) in bulk crystalline silicon (*c*-Si) makes it unsuitable for optoelectronic applications. Silica (SiO<sub>2</sub>) is another key material of the microelectronics industry; it has a bandgap of  $\sim 9$  eV. Optical-fiber technologies and metal-oxide-semiconductor field-effect transistors (MOSFETs) are based on (high-quality) silica. Molecular-beam epitaxy and chemical vapor deposition provide the needed growth technology for Si and SiO<sub>2</sub>. It is possible to combine crystalline silicon<sup>2,14-16</sup> and SiO<sub>2</sub> to produce structured materials having chemically pure, sharp, defect-free interfaces. The degree of advancement of the fabrication technology is such that the enhanced luminescence in Si/SiO<sub>2</sub> SLs cannot be explained only in terms of defects<sup>6</sup> and/or residual hydrogen atoms filling unsaturated Si dangling bonds—the latter being referred to as  $P_b$ -type centers<sup>17</sup>—located at the SL interfaces, as in the well-understood enhanced luminescence of hydrogenated *a*-Si.

The objective of the present article is to consider the detailed microscopic structure of the SiO<sub>2</sub>/Si/SiO<sub>2</sub> double interface structure and provide a first-principles understanding of the emission of light from Si/SiO<sub>2</sub> SL's. Only a few atomistic density functional theory (DFT) calculations on Si/SiO<sub>2</sub> SL's have been reported.<sup>18-23</sup> Many more would have been available were it not of the (naturally occurring) amorphous structure of SiO<sub>2</sub>: Amorphous structures require large supercells to get physically relevant results. Another important issue is the need to model the Si/SiO<sub>2</sub> interface so as to correctly incorporate the known experimental details. Recent core-level shift measurements<sup>24</sup> provide details of the suboxide (partially oxidized) Si atoms.<sup>25</sup> Further, the abruptness of the Si/SiO<sub>2</sub> interface has been established from trans-

mission electronic microscopy (TEM) experiments; values of the interface width as low as 5 Å have been reported.<sup>2,26</sup> Based on these observations, realistic Si/SiO<sub>2</sub> interface models have been designed by several workers.<sup>17,27–31</sup> Suboxide Si atoms in most of these models are distributed within three atomic layers of the Si/SiO<sub>2</sub> interface, corresponding to the lowest experimental interface thickness. Such interface models are needed for first-principles modeling of MOSFET's, and for SL structures, where *multiple* Si/SiO<sub>2</sub> interfaces are present.

An early (and tractable) Si/SiO<sub>2</sub> interface model was proposed by Herman and Batra.<sup>32</sup> The large lattice mismatch between SiO<sub>2</sub> and Si was accommodated by setting the  $\beta$ -cristobalite SiO<sub>2</sub> unit cell diagonally on the diamondlike *c*-Si unit cell. An oxygen atom was included in the interface to saturate the dangling bonds, resulting in a crystalline model of the interface. Another simple crystalline model, involving a bridge oxygen at the interface, was introduced by Tit and Dharma-wardana.<sup>33</sup> These models were studied using a variety of methods—tight-binding technique (TB),<sup>32,33</sup> full-potential, linear-muffin-tin-orbitals technique (FP-LMTO),<sup>20,21</sup> and linearized-augmented-plane-wave technique (FP-LAPW).<sup>22</sup> The dispersionless character of the band structure in the growth axis has been confirmed within all three theoretical approaches, thus demonstrating the existence of strong confinement. However, the nature of the energy gap—from both LMTO and LAPW calculations—is still indirect. Furthermore, these crystalline models show that the light absorption is quite dependent on the details of bonding and interface structure (bond lengths, angles, and chemical species), emphasizing the need for *more realistic, structurally relaxed* models.<sup>22</sup>

Several structurally relaxed models have been investigated by Kageshima and Shiraishi using first-principles methods. Their models were constructed starting from  $\beta$ -cristobalite as well as  $\alpha$ -quartz SiO<sub>2</sub> layers superposed onto *c*-Si layers with different possibilities for the Si/SiO<sub>2</sub> interface (such as hydrogen atoms at dangling bonds);<sup>19</sup> the atomic sites were then structurally relaxed. The calculations indicate that the energy gaps are indeed direct, and that interfacial Si–OH bonds are possible candidates for the light-emitting enhancement in SLs. However, the models are not consistent with the observed suboxide Si atomic distributions at the Si(001)/SiO<sub>2</sub> interfaces. For instance, no Si atoms bonded to three oxygens are present. Tit and Dharma-wardana<sup>34</sup> have constructed a partially relaxed model (PRM) starting from a structurally relaxed Si(001)/SiO<sub>2</sub> interface structure due to Pasquarello, Hybertsen, and Car (PHC).<sup>27</sup> This interface model contains all three suboxide Si atomic species. Hydrogen atoms were used by PHC to terminate the surface. In the Tit–Dharma-wardana model, the H atoms were removed and the Si/SiO<sub>2</sub> interface structure was converted into a SiO<sub>2</sub>/Si/SiO<sub>2</sub> double interface SL structure while preserving local tetrahedral bonding to obtain the PRM structure. Within the TB approach, the energy gap of the PRM was shown to be direct and enhancement of the optical absorption (as compared to *c*-Si) was confirmed.<sup>35</sup> This is further described in the next section, since the fully

relaxed models (FRM's) discussed in the present work are based on this PRM.

The results presented here go beyond the TB approach and were obtained within the projector-augmented-wave (PAW) theoretical framework. A brief description of the theory is given in Sec. II. The SL models were all structurally relaxed, and contain no hydrogen atoms at the interfaces. The interface suboxide Si atoms observed in experiment<sup>25</sup> arise naturally in the model. Calculations were carried out for different Si-layer thicknesses, in order to assess the effect of confinement on the electronic and optical properties. Supplementary models have been constructed to clarify the role of the suboxide atoms on the SL optical properties. We first review the theoretical methods (Sec. II), then focus on the four central issues needed to understand the Si/SiO<sub>2</sub> luminescence properties: construction of realistic interface models (Sec. III), quantum confinement (Sec. IV), role of the suboxide atoms (Sec. V), and optical effects associated with increased confinement (Sec. VI). Our study thus provides a complete, microscopic picture of the luminescence properties of Si/SiO<sub>2</sub> SL's.

## II. COMPUTATIONAL DETAILS

The electronic-structure calculations were carried out using the Vienna *ab initio* simulation package (VASP)<sup>36</sup> using the “frozen-core” PAW approach.<sup>37</sup> The overall framework is density-functional theory<sup>38,39</sup> (DFT) within the local-density approximation (LDA).<sup>40</sup>

The frozen-core PAW is a simpler form of the general PAW method introduced by Blöchl.<sup>41</sup> Blöchl's method is an extension of the usual LAPW<sup>42</sup> approach. Hence, the PAW method formally bridges the LAPW to the ultrasoft pseudopotentials (US-PP) in order to combine the precision of the former and the rapidity (for larger systems) of the latter. The PAW method has another advantage over the usual implementation of US-PP, essential for optical calculations: It avoids correcting for spatial nonlocality effects in typical pseudopotentials when evaluating the momentum operator  $\mathbf{p}$ . Further details can be found in the article of Adolph *et al.*<sup>43</sup>

Matrix elements of the momentum operator  $\mathbf{p}$  are needed for calculating interband optical effects. We describe the main steps that lead to the calculation of the absorption coefficient, starting from PAW solutions of the Kohn-Sham equations. The PAW approach rests on the following linear transformation:

$$|\Psi_N\rangle = |\tilde{\Psi}_N\rangle + \sum_i (|\phi_N\rangle - |\tilde{\phi}_N\rangle) \langle \tilde{p}_i | \tilde{\Psi}_N \rangle.$$

This relates the (calculated) pseudo wave function  $|\tilde{\Psi}_N\rangle$  to the (now corrected) all-electron wave function  $|\Psi_N\rangle$ . The index specifies the atomic site, angular momentum numbers and reference energy. The two functions  $|\tilde{\phi}_N\rangle$  and  $|\phi_N\rangle$  are, respectively, the pseudo-wave-function, and all-electron wave function of a reference atom. They are forced to overlap outside a given core region. The functions  $|\tilde{p}_i\rangle$  are the *projector* functions characteristic of the PAW method. Thus, the three functions  $|\phi_N\rangle$ ,  $|\tilde{\phi}_N\rangle$ , and  $|\tilde{p}_i\rangle$  constitute the frozen-core PAW data, being set prior to self-consistent field calcu-

lations. The projector functions  $|\tilde{p}_i\rangle$  are constructed so as to remain dual to the pseudo wave functions, to fulfill generalized orthogonality constraints and to remain (approximately) complete (see Ref. 43 for full definitions).

The application of the above linear transformation to any operator  $A$  within the PAW approach has been described by Blöchl [cf. Eq. (11) of Ref. 41]. If  $A$  is the momentum operator  $\mathbf{p}$  (in a certain direction defined by the polarization vector), we have

$$\langle\Psi_N|\mathbf{p}|\Psi_M\rangle=\langle\tilde{\Psi}_N|\mathbf{p}|\tilde{\Psi}_M\rangle+\sum_{i,j}\langle\tilde{\Psi}_N|\tilde{p}_i\rangle\langle\phi_i|\mathbf{p}|\phi_j\rangle-\langle\tilde{\phi}_i|\mathbf{p}|\tilde{\phi}_j\rangle\langle\tilde{p}_j|\tilde{\Psi}_M\rangle.$$

The imaginary part of the dielectric function,  $\epsilon_i$ , can be determined by using the Fermi golden rule within the Coulomb gauge; the expression becomes<sup>44</sup>

$$\epsilon_i(E)=\frac{\kappa^2}{E^2}\sum_{M,N}\int_{BZ}\frac{2d^3\vec{k}}{(2\pi)^3}|\langle\Psi_N|\mathbf{p}|\Psi_M\rangle|^2\times f_N(1-f_M)\delta(E_N-E_M-E),$$

where  $\kappa=2\pi e/m$ . The function  $f_n$  is the Fermi distribution and  $\langle\Psi_N|\mathbf{p}|\Psi_M\rangle$  are the PAW matrix elements. The whole expression corresponds to the probability per unit volume for a transition of an electron from the valence band state  $|\Psi_N\rangle$  to the conduction band state  $|\Psi_M\rangle$  to occur.

The tetrahedron method<sup>45</sup> is used to evaluate  $\epsilon_i(E)$ . The joint density of states, which determines the interband transitions  $\delta(E_N-E_M-E)$  and the optical matrix elements  $|\langle\Psi_N|\mathbf{p}|\Psi_M\rangle|^2$ , are computed on each tetrahedron (i.e.,  $1/4\times$  the sum of the matrix elements on the four corners of each tetrahedron). The real part  $\epsilon_r$  is then obtained using the Kramers-Kronig relation.<sup>44</sup> Since the dielectric function is the square of the complex refractive index,  $(\epsilon_r+i\epsilon_i)=(n_r+in_i)^2$ , the absorption coefficient becomes

$$\alpha(E)=4\pi\frac{E}{hc}n_i=4\pi\frac{E}{hc}\left[\frac{(\epsilon_r^2+\epsilon_i^2)^{1/2}-\epsilon_r}{2}\right]^{1/2}$$

with  $c$  the speed of light in vacuum,  $h$  Planck's constant, and  $E$  the photon energy.

Electron-hole ( $e$ - $h$ , excitonic) interactions were not included in the calculations, as they would be in, say, solutions

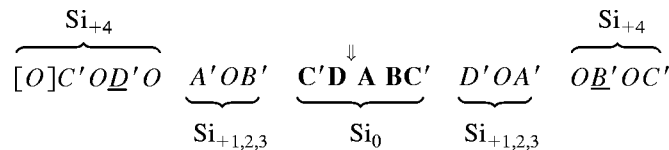
of the Bethe-Salpeter equation. The size of our systems prohibits such complete optical calculations, which are feasible only for very small systems (a few atoms). These additional effects would enhance the results from interband transitions since  $e$ - $h$  interactions generally increase the absorption at the onset.<sup>46</sup>

### III. CONSTRUCTION OF THE STRUCTURAL MODELS

Recent core-level shift experiments<sup>25</sup> have revealed the presence of all possible states oxidation for Si atoms in Si/SiO<sub>2</sub> structures such as SLs, that is Si <sup>$n$ +</sup>, where  $n=0,1,2,3,4$  is the charge found within each Si Wigner-Seitz sphere. Si<sup>0</sup> and Si<sup>4+</sup> are the charge states of Si found in bulk Si and bulk SiO<sub>2</sub>. The suboxide (subO) Si atoms with  $n=1,2,3$  are found at the interface. Slightly larger distributions for the subO Si<sup>3+</sup> densities, as compared to those for Si<sup>1+</sup> and Si<sup>2+</sup>, were reported in these experiments. Microscopic Si/SiO<sub>2</sub> interface models should be consistent with experiments in closely reproducing the density distributions of *all* subO Si atoms.

As mentioned above, the Si/SiO<sub>2</sub> SL model structures discussed in the present article are based on the Si(001)/SiO<sub>2</sub> interface structures obtained by PHC,<sup>27</sup> who used the Car-Parrinello method to relax the models to their energy minima. It is important to note that the PHC models were *not* designed for the double interface structure found in SiO<sub>2</sub>/Si/SiO<sub>2</sub> SL's but, rather, for a single Si/SiO<sub>2</sub> interface which terminates into the vacuum; this is done by saturating dangling bonds with H atoms. Thus, these models *de facto* contain the essential details of atomic positions and charge states at the Si/SiO<sub>2</sub> interface.

Tit and Dharma-wardana<sup>34</sup> have generated a Si/SiO<sub>2</sub> SL structure starting from one of the PHC models that contains an *equal* distribution of the three subO atoms, in (almost complete) accord with experiment. This SL model has been constructed by first operating a mirror transformation and then a partial rotation of the Si/SiO<sub>2</sub> section of the relaxed interface structure, leading to an intermediate Si/SiO<sub>2</sub> [mirror] SiO<sub>2</sub>/Si SL structure. Second, some of the Si layers were inverted in order to meet the  $sp^3$ -bonding topology. The resulting Si/SiO<sub>2</sub> SL's structure, fully described in the article of Tit and Dharma-wardana,<sup>34</sup> has the following final configuration:



The connection between the symbols in this configuration and the specific atomic layers in the model is shown in Fig. 1. The letters  $A, B, C$ , and  $D$  correspond to silicon atomic layers, while the  $O$ 's are oxygen layers. The primes denote

layers that depart from the diamondlike-Si crystalline arrangement, and  $[O]$  corresponds to the layer where the mirror operation has been performed.  $B'$  and  $D'$  are the Si layers which have been inverted in order to satisfy the  $sp^3$ -bonding

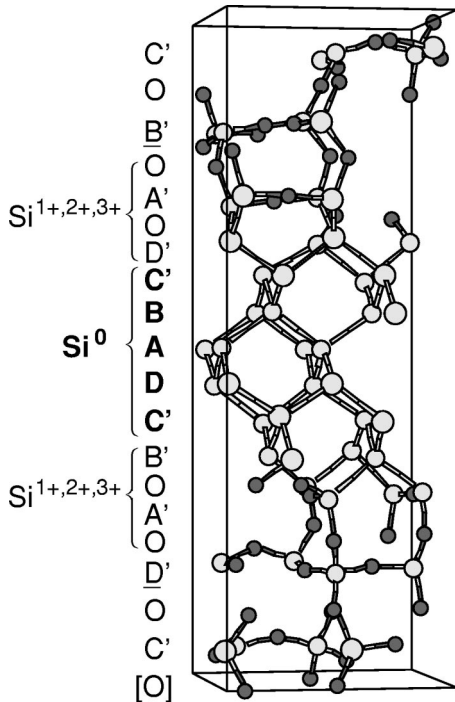


FIG. 1. The unit cell of the fully relaxed SL model (FRM1). The configuration of the bulklike and suboxide Si atomic planes is also depicted. The white and black circles are, respectively, the positions of Si and O atoms.

topology. The subO  $\text{Si}^{n+}$  atoms, with  $n=1,2,3$ , are distributed within only two Si layers, while the  $\text{Si}^0$  atoms are distributed within five atomic layers. The embryonic PHC interface model corresponds roughly to one side of the above configuration, starting from the arrow up to the right.

Of course, this construction induces artificial symmetries in the middle of the  $\text{SiO}_2$  layer (more precisely, upon and around the  $[O]$  layer); this model is thus in essence *partially* relaxed—the PRM referred to earlier. Significant information on the electronic and optical properties of this model have been extracted, within the TB approach, by Tit and Dharma-wardana,<sup>34</sup> who obtained direct energy gaps as well as dispersionless band structures. Furthermore, the imaginary part of the dielectric function was calculated, and then the absorption coefficient was deduced. From this calculation, enhancement of absorption as well as blueshift with confinement have been demonstrated.<sup>35</sup>

The next obvious step is to relax the PRM, i.e., determine the set of positions which leads, via the Hellman-Feynman forces, to the lowest total energy. We have used the PAW approach described in the previous section to obtain a first fully relaxed model (FRM1), which contains approximately one unit cell of confined Si. The supercell contains 52 Si and 44 O atoms, and has dimensions  $7.675 \times 7.675 \times 24.621 \text{ \AA}^3$ . The relaxation procedure has been performed with five  $\mathbf{k}$  points in the reduced Brillouin zone (BZ). The energy cutoff was 25.96 Ry in all calculations. The total energy was found to decrease by 30.84 eV (0.32 eV per atom) during relaxation. Figure 2 shows the bondlength distributions before (PRM) and after (FRM1) relaxation; the bond lengths are

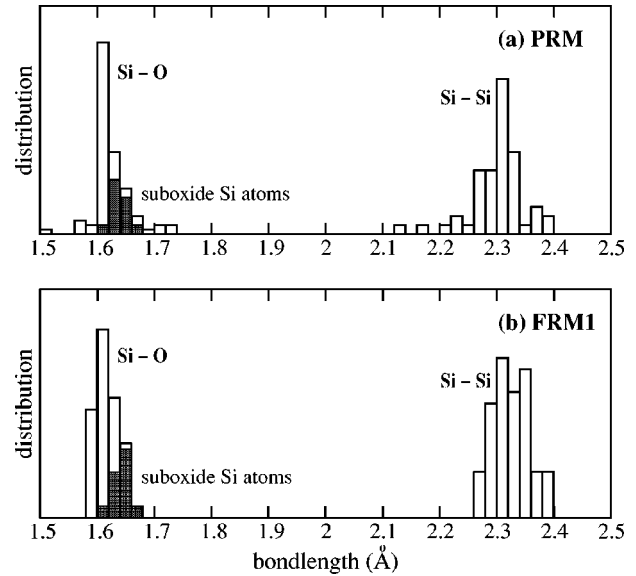


FIG. 2. Evolution of the Si-O and Si-Si bond lengths from (a) the PRM construction by Tit and Dharma-wardana, to (b) the fully relaxed structure (FRM1) described in the text.

centered around the expected values, viz.,  $\sim 1.61 \text{ \AA}$  for Si-O and  $2.35 \text{ \AA}$  for Si-Si bonds. The shaded boxes in Fig. 2 are the distributions of the interface subO Si atoms, while the empty boxes are the total distribution bond lengths, including subO Si atoms; the shaded boxes remain relatively unchanged upon relaxation since both interfaces were already at their energy minimum, after PHC. The main atomic drift during relaxation occurs in the center of the Si and  $\text{SiO}_2$  layers, i.e., near the  $[O]$  and the A layer of the configuration discussed above. Interfacial Si-O bond lengths of all subO Si atoms depart from the values of  $\text{Si}^{4+}$  in the  $\text{SiO}_2$  layer. The broadening of the Si-Si bond lengths is in general much larger than that of Si-O; the distortion of the bond lengths are thus mainly within the Si layer and at the Si/ $\text{SiO}_2$  interface, i.e., not inside the silica layer. This is further discussed below. The resulting FRM1 is shown in Fig. 1.

Additional models having thicker Si wells were constructed in order to examine the role of subO Si layers and the effect of confinement on the electronic and optical properties. As noted earlier, the FRM1 structure contains approximately one unit cell of confined Si, i.e., the set of layers with charge state  $\text{Si}^0$  (bulklike Si). By inserting one, then two, additional ABCD Si atomic planes (i.e., one Si unit cell, thickness  $5.43 \text{ \AA}$ ), and relaxing all atoms, we generated two additional models—FRM2 and FRM3. The FRM2 contains 68 Si atoms while the FRM3 has 84 Si atoms; both have 44 oxygen atoms, as in the FRM1. The *total* energy variation for the FRM2 during relaxation was found to be only 0.15 eV (i.e., 0.0013 eV/atom) while for the FRM3, this change is a minuscule 0.051 eV (i.e., 0.00040 eV/atom). These numbers imply that both FRM2 and FRM3 have essentially crystalline Si layers. The FRM2 has nine  $\text{Si}^0$  atomic planes while the FRM3 has thirteen.

Figure 3 shows the distributions of the Si-Si bond lengths in the FRM3, starting from the  $\text{Si}(001)/\text{SiO}_2$  interfaces (at the bottom of Fig. 3) and going towards the center of the

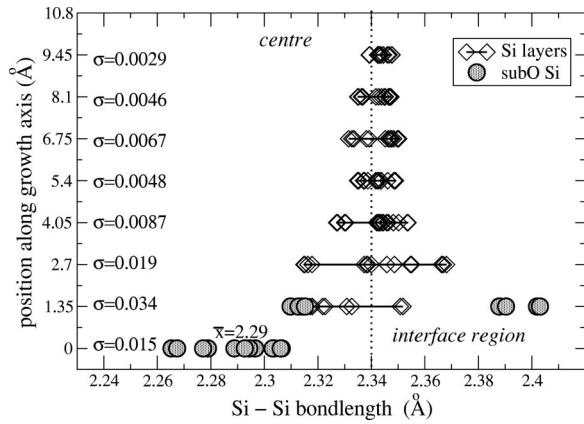


FIG. 3. Si-Si bond length distribution in the FRM3, from the interface (bottom of figure) towards the center (top of figure) of the Si layer. (There are thirteen  $\text{Si}^0$  layers in the FRM3 and thus six interplanar Si-Si bond lengths starting from both interfaces towards the center of the Si layer.)

silicon layer along the growth axis. The standard deviation ( $\sigma$ ) from the mean value ( $\bar{x} = 2.34 \text{ \AA}$  in all atomic layers except at the interface, where  $\bar{x} = 2.29 \text{ \AA}$ ) is also given. The diamond-shaped symbols correspond to the Si-Si bond lengths for  $\text{Si}^0$  atoms while the filled circles are subO Si-Si bond lengths at the interfaces. The Si-Si bond lengths depart significantly from their crystalline counterparts at the interfaces up to about three atomic layers, where  $\sigma = 0.019$ ; the standard deviation is four times higher at the interfaces than in the fifth atomic layer. This deviation of the bond lengths at the Si/SiO<sub>2</sub> interfaces shows that it is important to take relaxation aspects into account. Indeed, amorphous SiO<sub>2</sub> layers in realistic SL's induce strain and disorder in the Si layer, as confirmed in Fig. 3. This effect could generate localized defects giving rise to efficient radiative electron-hole recombination. However, the strain fields only contribute to the small *quasimomenta* regime and cannot easily supply the momentum deficit involved in the indirect transition of *c*-Si. Moreover, the relatively small size of our supercell models in the *x*-*y* directions prevents firm conclusions being drawn about the influence of this strain on the optical properties. Further aspects of the role of interfaces are discussed in Sec. V.

The three subO Si configurations at the interfaces of the FRMs are shown in Fig. 4 with their corresponding bond lengths. Note that the left and right interfaces in the SiO<sub>2</sub>/Si/SiO<sub>2</sub> SLs are not *exactly* equivalent; they remain independent (during structural relaxation, for instance). However, a subO Si on the left interface has a locally equivalent subO Si on the right interface, by construction. As a consequence, each pair of equivalent subO Si atoms have approximately the same bond lengths and angles in all the FRMs. As seen in Fig. 4, the bond lengths depart from their bulk values, which are 2.35 Å for *c*-Si and 1.61 Å for SiO<sub>2</sub>. In addition, the angles of the subO Si tetrahedra vary considerably: The Si-Si-Si angles vary from 99° to 125°, the O-Si-Si angles vary from 96° to 126°, while all O-Si-O angles remain around 106°. It is thus clear that the subO Si tetrahedra at the interfaces are distorted as compared to bulk-Si tetrahedra.

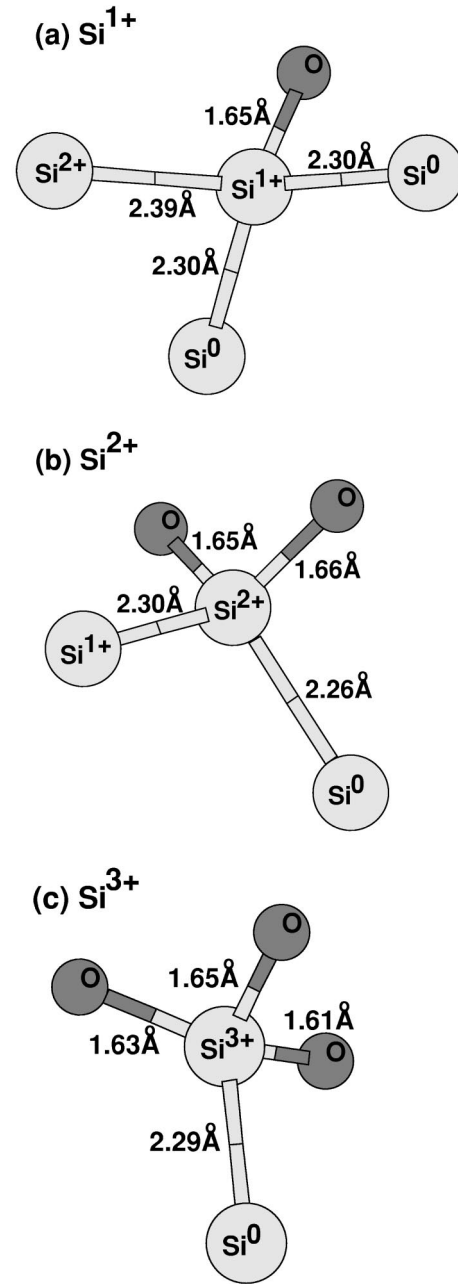


FIG. 4. Structure of the three suboxide interfacial Si atoms.

As discussed later on, the role of subO Si atoms was further studied using the following variations of the FRM2: First, we removed all  $\text{Si}^{4+}$  atoms and attached the proper number of hydrogen atoms to neutralize the excess charges. The H positions were then relaxed while keeping all the silicon and oxygen atoms fixed. This structure thus contains  $\text{Si}^0$  atoms and  $\text{Si}^{n+}$  subOs, where  $n = 1, 2, 3$  (i.e.,  $n \neq 4$ ). A variation of this structure was generated by removing all oxygen atoms and filling the Si dangling bonds with H atoms, and again relaxing the H atoms. The final Si-H bond lengths vary from 1.47 Å to 1.53 Å, after relaxation. This final structure is thus subO-free and contains only  $\text{Si}^0$  atoms, except at the interface with the vacuum, where hydrogen atoms fill the dangling bonds. These three confinement models are shown

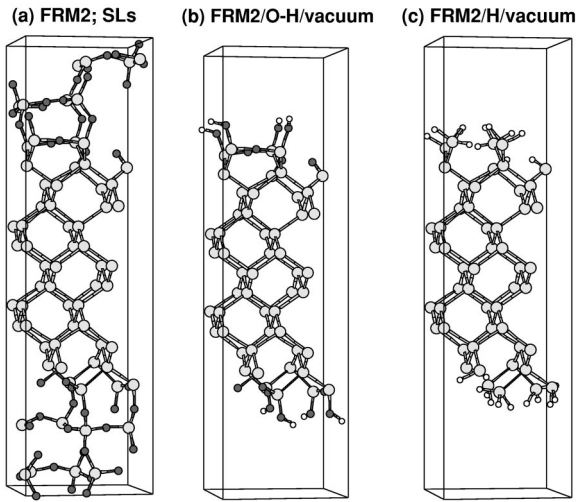


FIG. 5. (a) The FRM2 SL's (b) the FRM2/O-H/vacuum model (c) the FRM2/H/vacuum model.

in Fig. 5; they will be referred to as FRM2, FRM2/O-H/vacuum, and FRM2/H/vacuum, respectively.

In Fig. 6 we show the BZ of the supercell, the standard *c*-Si diamond BZ, and the high symmetry axes used for the band structure calculations. We also constructed the bulk *c*-Si structure in a supercell of dimensions similar to that of the FRM SL's, so that comparisons can be done within the same **k**-space zone scheme. This will be used in the next three sections for comparisons of band structure as well as absorption calculations.

IV. QUANTUM CONFINEMENT

In this section, we discuss the nature of the confined states in the SL's. We calculated the band structures of the three SL models—FRM1, FRM2, and FRM3—as well as the supplementary FRM2/O-H/vacuum structure, cf. Fig. 5(b). The latter is the “ultimate” in terms of confinement, as the two interfaces with vacuum constitute infinite potential walls. All band structures are analyzed and compared within equivalent

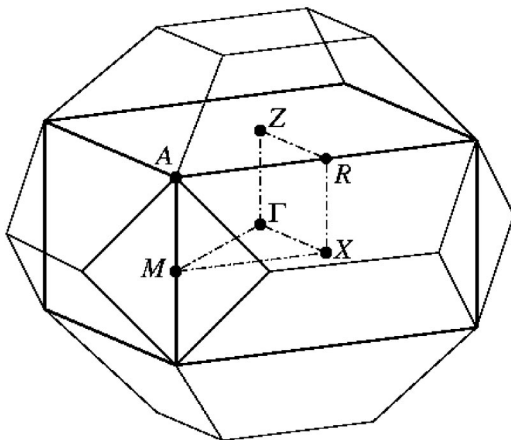


FIG. 6. Definition of the SLs BZ superposed to the diamondlike BZ. The principal axis used for band structure calculation are also depicted.

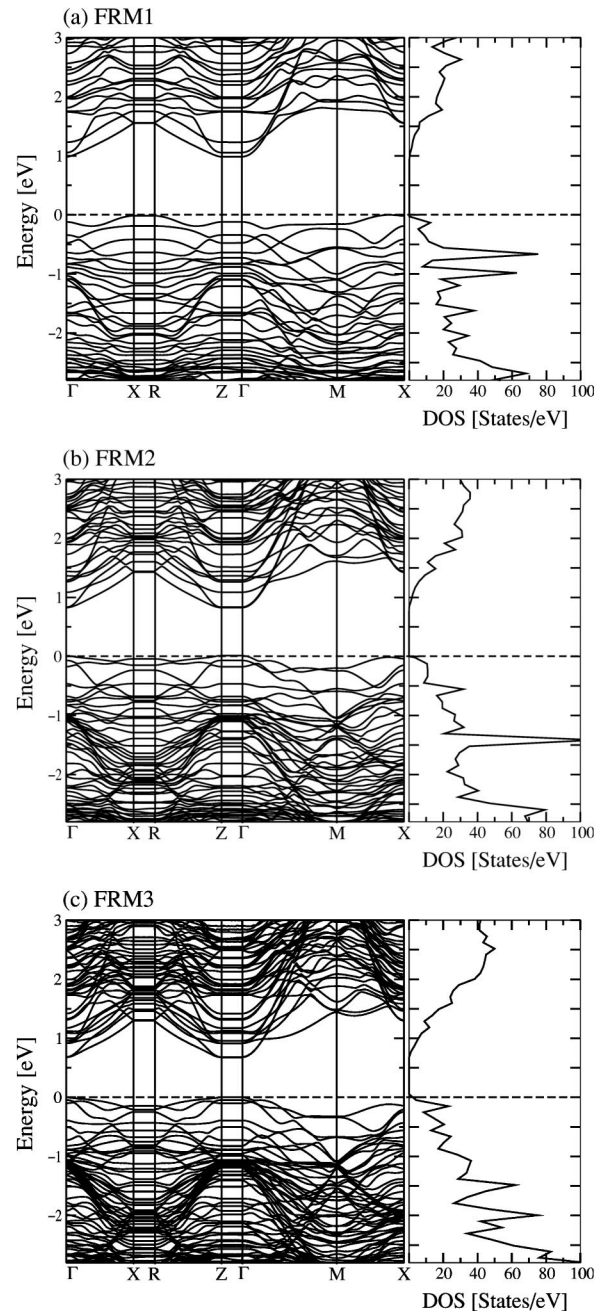


FIG. 7. Band structures and density of states (DOS) of the three SL models. The DOS are calculated using  $(7 \times 7 \times 1)$  **k**-point grid, which corresponds to 144 irreducible tetrahedra.

supercell BZ. The growth axis of the SL's being the *z* axis, confinement effects are expected to take place in the *X*-*R* and *Z*- $\Gamma$  axis of the BZ (see Fig. 6 for axis definitions).

The band structures of the three SL's and their total density of states (DOS) are shown in Fig. 7. We find that the band structures in the growth axis (*X*-*R* and *Z*- $\Gamma$ ) are dispersionless, for all models and all energies. In physical terms, dispersionless band structures imply infinite effective masses, reflecting the strong confinement. The DOS have a more abrupt variation in the valence bands than in the conduction bands. However, DOS alone are not enough to fully

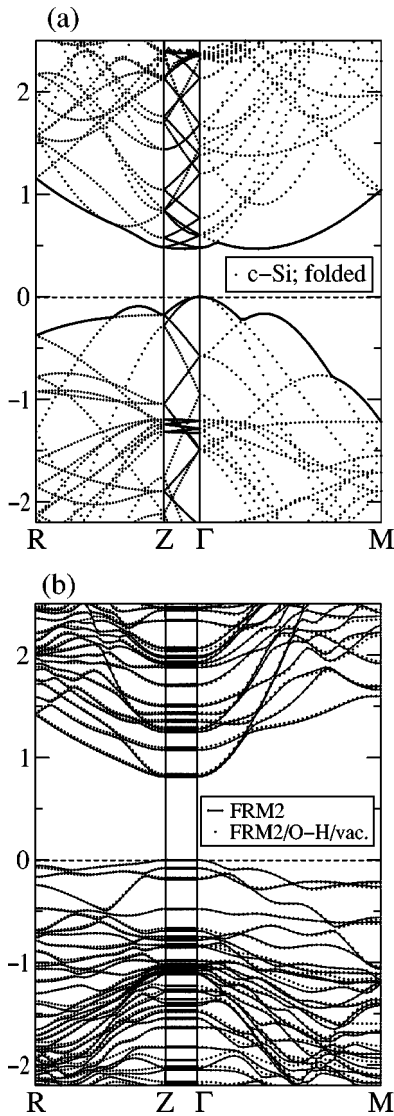


FIG. 8. Band structures of (a)  $c$ -Si in the (folded) SL BZ (b) comparison between the FRM2 SL's and the FRM2/O-H/vacuum band structures.

understand the optical processes involving the interband transitions, since the weighting of the optical matrix elements is needed. This is further discussed in Sec. VI.

Let us consider in more details one of the SL models, namely the FRM2. We select the  $R$ - $Z$ - $\Gamma$ - $M$  high-symmetry axis where the major features, viz. the relevant energy gaps, appear. The band structures of the folded  $c$ -Si structure, the FRM2 SL's structure as well as the FRM2/O-H/vacuum structure, have been calculated and compared. Figures 8(a) and (b) contain a synopsis of all calculations for  $\mathbf{k}$  points along  $R$ - $Z$ - $\Gamma$ - $M$ . Several conclusions can be drawn from these figures.

By comparing the bands for  $c$ -Si, Fig. 8(a), with those for the FRM2 SL, Fig. 8(b) (solid lines), we see that folding effects cannot by themselves explain the new band structure. The bands in the  $Z$ - $\Gamma$  directions are totally modified by the confinement. Although  $c$ -Si always has an optically indirect band gap, this band gap becomes almost direct in its folded

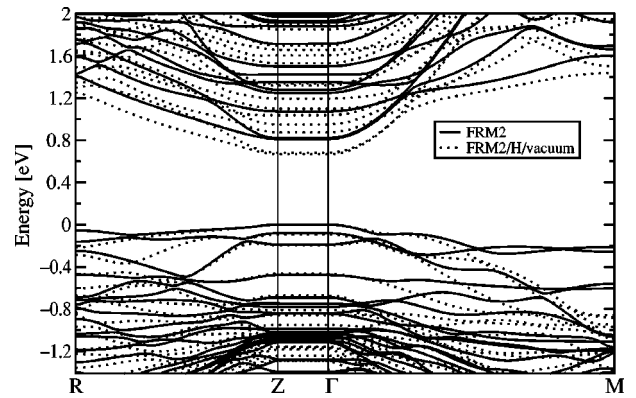


FIG. 9. Comparison of the band structures for FRM2/H/vacuum and FRM2 SL's.

configuration, as can be seen from Fig. 8(a), while for the SL the band gap is *unequivocally* direct, and significantly increased. Moreover, comparing the bands in a direction orthogonal to the growth axis, for instance around  $M$  in both Figs. 8(a) and (b), we see that the valence bands are raised; the lowest conduction band in the  $\Gamma$ - $M$  direction is pushed to higher energies. In addition, they exhibit less dispersion in the SL than in  $c$ -Si, in general. Hence, confinement modifies the electronic properties in the growth axis as well as in directions orthogonal to it. This is further analyzed from optical absorption calculations, below.

We compare in Fig. 8(b) the band structures of the FRM2 and FRM2/O-H/vacuum models. The positions of the  $\text{Si}^0$  atoms, as well as the subO Si in the two structures, are identical. The solid lines displays the band structures of the FRM2, while the dots display the bands of the FRM2/O-H/vacuum structure. It is clear that the two band structures are nearly identical. This calculation shows that the  $\text{SiO}_2$  layers act as virtually impenetrable barriers. The electronic properties of hypothetical SL structures having only subO Si—i.e., no  $\text{Si}^{4+}$  of  $\text{SiO}_2$ —and positioned at the subO Si sites, would give nearly identical electronic properties as Si/SiO<sub>2</sub> SL's, for energies close to the band gap. Our calculations show that the electronic wave functions die out at the suboxide Si atoms of the interfaces. Thus the barrier is sharply located just behind the subO Si atoms, and therefore just two atomic layers could be used as a barrier without altering the electronic properties, when energies involved (in the device) remain close to the energy gap. The influence of the interface subO Si atoms is further analyzed next.

## V. ROLE OF INTERFACES

In order to assess the role of the subO ions on the electronic properties, we calculated the band structures of the FRM2/H/vacuum structure, Fig. 5(c), which contains *no* subO Si; the dangling bonds have been filled by hydrogen atoms and hydrogen atoms (only) have been structurally relaxed. Figure 9 summarizes the results. The LDA band gap is still direct but significantly lowered, from 0.81 eV in the FRM2 to 0.67 eV in the FRM2/H/vacuum structure. Interface reconstruction (as discussed in Sec. III and Fig. 3) thus has significant impact on the electronic properties. The bands

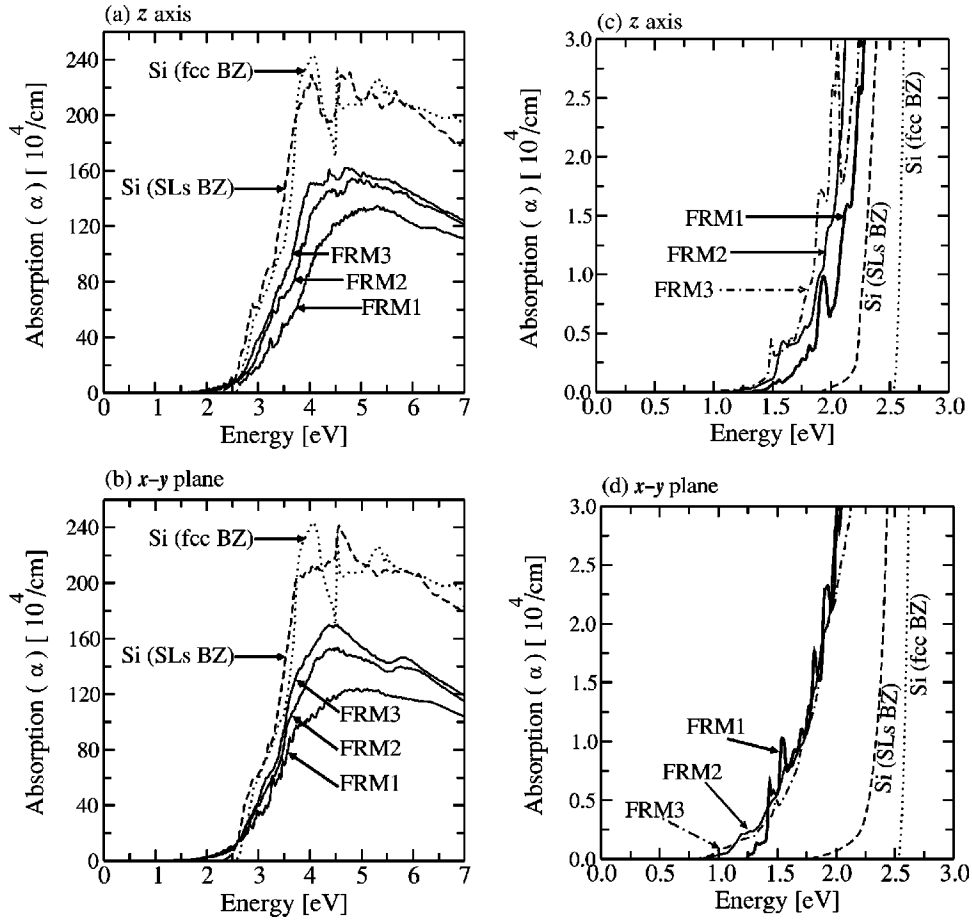


FIG. 10. Absorption coefficient of the SL models as compared to *c*-Si. (a) and (c) are the absorption in the growth axis; (b) and (d) are the absorption in the plane orthogonal to the growth axis.

in the plane orthogonal to the growth axis are quite different from FRM2; e.g., the valence band is lowered near the *M* and *R* points, becoming similar to the *c*-Si band structure. We thus conclude that the subO Si atoms have two effects: (i) increase the band gap and (ii) produce dispersionless valence bands. The charge states in the subO are responsible for the increase in the band gap, while the strongly increased valence-band offset leads to essentially dispersionless bands.

## VI. BLUESHIFT AND OPTICAL ENHANCEMENT

The matrix elements entering the calculations of the optical properties are often approximated as a constant in a given range of energies. However, such an approximation is inadequate for elucidating the enhanced luminescence in Si/SiO<sub>2</sub> SL's. This section deals with calculating the absorption coefficient within the Fermi golden rule and interband-transition theory.

Since the Si-layer thickness  $L_{\text{Si}}$  is relevant to the energy shift in SL's, this quantity needs first to be defined. This involves some uncertainty associated with the interface thicknesses  $L_{\text{subO}}$ .

The interface thickness  $L_{\text{subO}}$  was estimated to be  $\sim 1.60$  Å from our calculations of the subO Si region. This is

the largest distance (projected onto the *z* axis) between any two subO Si atoms. Hence the upper bound to  $L_{\text{Si}}$  are 11.17 Å, 16.58 Å, and 22.01 Å for the FRM1, FRM2, and FRM3, respectively, while the lower-bound thicknesses are simply  $L_{\text{Si}} - 2L_{\text{subO}}$ . We define the Si thickness in the SL's to include the interface subO Si atoms as well (corresponding to the upper bound). This choice is made since subO Si ( $\text{Si}^{1+}$ ,  $\text{Si}^{2+}$ , or  $\text{Si}^{3+}$ ) atoms contribute to the electronic properties, as do bulk-Si atoms ( $\text{Si}^0$  atoms); for instance, we showed above [see, e.g., Fig. 8(b)] that the band structures of the FRM2 SLs and the FRM2/O-H/vacuum systems overlap, and indicated where the effective barrier begins.

The band gaps of the FRM1, FRM2, and FRM3 (see the band structures in Fig. 7) are direct except for the FRM1 where the band gap is *nearly* direct with only 0.12 eV between the direct and indirect transitions. The values of the gap are 0.99 eV, 0.81 eV, and 0.68 eV for the FRM1, FRM2, and FRM3, respectively. The direct transition at  $\Gamma$  for the FRM1 equals 1.11 eV. For the FRM2 and the FRM3, the band gaps are direct and located on the whole *Z*- $\Gamma$  axis [see Figs. 7(b) and (c)]. Direct transitions can thus be achieved between the valence band and the conduction band, along the *Z*- $\Gamma$  line of the BZ. We thus obtain, under the LDA, a blue-shift

$$0.68 \text{ eV} \rightarrow 0.81 \text{ eV} \rightarrow 0.99 \text{ eV}$$

with increased confinement

$$2.2 \text{ nm} \rightarrow 1.7 \text{ nm} \rightarrow 1.1 \text{ nm}.$$

However, these values for the energy gaps are much lower than the experimental ones. It is well known that DFT within the LDA underestimates the energy gaps of semiconductors and insulators. For *c*-Si, the DFT-LDA gap is approximately 0.6 eV less than the experimental value. For the  $\beta$ -cristobalite phase of SiO<sub>2</sub>, in the group  $I\bar{4}2d$ , the DFT-LDA energy gap is 5.8 eV while the experimental value is about 3 eV higher, i.e.,  $\sim 9$  eV. Approximate, but realistic, band gaps can be obtained by adding 0.6 eV overall:

$$1.28 \text{ eV} \rightarrow 1.41 \text{ eV} \rightarrow 1.59 \text{ eV}.$$

$$(2.2 \text{ nm}) \quad (1.7 \text{ nm}) \quad (1.1 \text{ nm})$$

These energy gaps correspond to the lower bound of the experiments<sup>3</sup> and lie in the visible spectrum. However, these gaps are still somewhat lower than the experimental values.<sup>1,2,4-6</sup> The discrepancy can be explained by recrystallization processes, which lead to the formation of nanoclusters that would increase the confinement, and correspondingly the measured energy gaps.<sup>47</sup> The analysis of such a behavior, which is beyond the scope of the present work, would require zero-dimensional-confined model structures.

The absorption of the three SL models and *c*-Si have been calculated both in the diamond-like BZ and in the SL BZ. For *c*-Si in the diamondlike BZ, we used  $(20 \times 20 \times 20)$  **k** points,<sup>43</sup> while in the SL BZ,  $(7 \times 7 \times 2)$  **k** points are used. Calculations using more **k** points, viz.  $(8 \times 8 \times 3)$ , show that  $(7 \times 7 \times 2)$  is quite sufficient to recover the form of the absorption curve for all the SL models. The purpose of calculating the absorption of *c*-Si in two different BZ's is to estimate errors, first due to zone folding effects (which cause round-off errors, leading to non-absolutely-null transitions at the onset)<sup>48</sup> and, second, to the tetrahedron method itself which needs large amounts of **k** points. The broadening in the absorption curves has been fixed to 0.015 eV for all the absorption curves discussed below, as suggested by Fuggle.<sup>24</sup>

Figure 10 shows the absorption results. Panels (a) and (b) give an overall view of the absorption curves for the *z* axis in (a) and the *x*-*y* plane in (b). Panels (c) and (d) show the absorption at the onset, for the *z* axis in (c) and the *x*-*y* plane in (d). In all cases, we included the absorption of *c*-Si calculated in the diamond-like BZ, as well as the one in the SL BZ. Direct comparison of the two *c*-Si absorption curves give an estimate of imprecisions due to zone foldings and intermediate number of **k**-point effects. It shows that the absorption is slightly underestimated in the SL calculations; e.g., in Fig. 10(c), the onset of absorption of *c*-Si in the SL BZ takes place at 2.0 eV while in the diamondlike BZ the onset happens at the correct value of 2.52 eV (which is for *c*-Si the LDA direct transition at  $\Gamma$ ). This numerical effect cannot be avoided and will arise, as well, in any Si/SiO<sub>2</sub> supercell. Hence, all comparison of the SL absorption must

be made with *c*-Si calculated in the equivalent SL BZ, i.e., within equivalent **k**-space zone schemes.

Since the SLs are fabricated with the objective of changing the indirect gap to a direct gap, we now discuss the absorption threshold region. Comparison at the onset of absorption from Figs. 10(c) or (d) shows that all absorption curves have a lower energy threshold than *both* the *c*-Si absorption curves, and especially below the one calculated in the equivalent SL BZ having equal number of **k** points. That is, *the SL's show absorption (and emission) in the spectral region above the indirect gap of c-Si and below the direct gap of c-Si.* This shows that the absorption in *all* confined Si/SiO<sub>2</sub> SL models is enhanced, compared to *c*-Si; the transitions are direct in SL's and have an active oscillator strength. For the folded *c*-Si energy bands, the lower bands above the Fermi level, and the corresponding oscillator strength, remain dark; in other words, the optical matrix elements of the SL BZ of *c*-Si are null up to  $\sim 2.0$  eV. This result clearly demonstrates the enhancement of the absorption (and emission) mechanisms in confined Si structures. Furthermore, upon inspection of the absorption curves in the plane orthogonal to the growth axis [Fig. 10(d)], we note that the energy thresholds of the absorption are all below *c*-Si: thus, the *x*-*y* absorption of the FRM's takes place approximately at their respective direct energy gaps, and then behave in a similar manner, as expected from the similarity of the SL band structures, in this plane.

We examine, finally, the higher-energy region which corresponds to the usual direct transition (3–6 eV) in *c*-Si. Even here, Fig. 10(a) demonstrates a blueshift with increased confinement in the *z* axis. The overall absorption maxima for FRM1–FRM3 are at 5.28 eV, 4.83 eV, and 4.71 eV, with intensities of 136, 155, and 162 ( $\times 10^4$ /cm), respectively. For *c*-Si in the SL BZ (to ensure comparable precision in the calculations) the second peak, i.e., the maximum, take place at 4.70 eV (with absorption equal to  $231 \times 10^4$ /cm), while the first peak is at 4.0 eV (and with absorption equal to  $229 \times 10^4$ /cm). We emphasize that there is still a slight blueshift in the *x*-*y* plane orthogonal to the growth axis, but less pronounced than in the growth axis.

## VII. CONCLUDING REMARKS

In this work, the structural, electronic, and optical properties of Si/SiO<sub>2</sub> superlattices have been studied on the basis of structurally relaxed models. These SL models, which contain no hydrogen atoms at the Si/SiO<sub>2</sub> interfaces, exhibit enhanced optical absorption/emission, as observed in experiment; this can be attributed to the presence of silicon dioxide barriers. In experiments performed under ultrahigh vacuum conditions, the oxidization process would predominantly give rise to oxide bonds at the interfaces, but still, few hydrogen atoms are expected to be present and fill some of the remaining dangling bonds.

Our calculations show that the oxide barriers are central to the optical enhancement in SL's. It is well known that hydrogen atoms play a similar role in amorphous silicon by filling dangling bonds. This suggests that it might also be the case in Si/SiO<sub>2</sub> SL's, where hydrogen atoms fill extra dan-

gling bonds, and thus would amplify the optical enhancement effect already exerted by the oxide barriers. Further studies are needed to ascertain this.

We have shown that suboxide Si atoms at the interfaces act as virtually impenetrable barriers. The active barrier thickness thus corresponds to the suboxide Si layer—only 1.6 Å in our models. The confined Si layer thus consists of bulk Si *and* suboxide Si atoms. Suboxide Si atoms at the interfaces modify the electronic properties in two manners: They (i) increase the energy gap and (ii) lead to dispersionless band structures, which increases the transition probabilities.

Other confinement models (zero-dimensional structures) and interface effects will be considered in future work. For instance, inclusion of other atomic species—such as nitrogen that would generate subnitric Si atoms at the Si/SiO<sub>2</sub>

interface—are expected to modify the electronic properties, and hence enhance the optical absorption/emission spectra.

#### ACKNOWLEDGMENTS

It is a pleasure to thank Dr. Jurgen Furthmüller for help with the optical calculations in VASP. We gratefully acknowledge Dr. Zheng-Hong Lu for helpful discussions and suggestions. This work is supported by grants from the Natural Sciences and Engineering Research Council (NSERC) of Canada and the “Fonds pour la formation de chercheurs et l’aide à la recherche” (FCAR) of the Province of Québec. We are indebted to the “Réseau québécois de calcul de haute performance” (RQCHP) for generous allocations of computer resources.

\*Author to whom correspondence should be addressed: Email address: laurent.lewis@umontreal.ca

<sup>1</sup>Z.H. Lu, D.J. Lockwood, and J.-M. Baribeau, *Nature (London)* **378**, 258 (1995).

<sup>2</sup>Y. Kanemitsu and S. Okamoto, *Phys. Rev. B* **56**, R15 561 (1997).

<sup>3</sup>S.V. Novikov, J. Sinkkonen, O. Kilpelä, and S.V. Gastev, *J. Vac. Sci. Technol. B* **15**, 1471 (1997).

<sup>4</sup>L. Khriachtchev, M. Räsänen, S. Novikov, O. Kilpelä, and J. Sinkkonen, *J. Appl. Phys.* **86**, 5601 (1999).

<sup>5</sup>V. Mulloni, R. Chierchia, C. Mazzeleni, G. Pucker, L. Pavesi, and P. Bellutti, *Philos. Mag. B* **80**, 705 (2000).

<sup>6</sup>Y. Kanemitsu, M. Liboshi, and T. Kushida, *Appl. Phys. Lett.* **76**, 2200 (2000).

<sup>7</sup>L.T. Canham, *Appl. Phys. Lett.* **57**, 1046 (1990).

<sup>8</sup>V. Lehman and U. Gösele, *Appl. Phys. Lett.* **58**, 856 (1991).

<sup>9</sup>L. Tsyberkov, K.L. Moore, D.G. Hall, and P.M. Fauchet, *Phys. Rev. B* **54**, R8361 (1996).

<sup>10</sup>S. Cheylan and R.G. Elliman, *Appl. Phys. Lett.* **78**, 1912 (2001).

<sup>11</sup>W.L. Ng, M.A. Lourenço, R.M. Gwilliam, S. Ledain, G. Shao, and K.P. Homewood, *Nature (London)* **410**, 192 (2001).

<sup>12</sup>P. Schmuki, L.E. Erickson, and D.J. Lockwood, *Phys. Rev. Lett.* **80**, 4060 (1998).

<sup>13</sup>S. Schuppler, S.L. Friedman, M.A. Marcus, D.L. Adler, Y.-H. Xie, F.M. Ross, Y.J. Chabal, T.D. Harris, L.E. Brus, W.L. Brown, E.E. Chaban, P.F. Szajowski, S.B. Christman, and P.H. Citrin, *Phys. Rev. B* **52**, 4910 (1995); D.J. Lockwood, A. Wang, and B. Bryskiewicz, *Solid State Commun.* **89**, 587 (1994).

<sup>14</sup>Z.H. Lu and D. Grozea, *Appl. Phys. Lett.* **80**, 255 (2002).

<sup>15</sup>M. Zacharias, J. Bläsing, K. Hirschman, L. Tsybeskov, and P.M. Fauchet, *J. Non-Cryst. Solids* **266-269**, 640 (2000).

<sup>16</sup>M. Zacharias, J. Bläsing, P. Veit, L. Tsybeskov, K. Hirschman, and P.M. Fauchet, *Appl. Phys. Lett.* **74**, 2614 (1999).

<sup>17</sup>A. Stirling, A. Pasquarello, J.-C. Charlier, and R. Car, *Phys. Rev. Lett.* **85**, 2773 (2000).

<sup>18</sup>B. Delley and E.F. Steigmeier, *Appl. Phys. Lett.* **67**, 2370 (1995).

<sup>19</sup>H. Kageshima and K. Shiraishi, in *Materials and Devices for Silicon-Based Optoelectronics*, edited by J.E. Cunningham, S. Coffa, A. Polman, and R. Soref, *Mater. Res. Soc. Symp. Proc.* No. 486 (Material Research Society, Pittsburgh, PA, 1998), p. 337.

<sup>20</sup>M.P.J. Pukkinen, T. Korhonen, K. Kokko, and I.J. Väyrynen, *Phys. Status Solidi A* **214**, R17 (1999).

<sup>21</sup>E. Degoli, and S. Ossicini, *Surf. Sci.* **470**, 32 (2000).

<sup>22</sup>P. Carrier, L.J. Lewis, and M.W.C. Dharma-wardana, *Phys. Rev. B* **64**, 195330 (2001).

<sup>23</sup>B.K. Agrawal and S. Agrawal, *Appl. Phys. Lett.* **77**, 3039 (2000).

<sup>24</sup>J.C. Fuggle, in *Unoccupied Electronic States*, Vol. 69 of Topics in Applied Physics, edited by J.C. Fuggle and J.E. Inglesfield, (Springer-Verlag, Berlin, 1992).

<sup>25</sup>M.T. Sieger, D.A. Luh, T. Miller, and T.-C. Chiang, *Phys. Rev. Lett.* **77**, 2758 (1996); Z.H. Lu, M.J. Graham, D.T. Jiang, and K.H. Tan, *Appl. Phys. Lett.* **63**, 2941 (1993); F.J. Himpsel, F.R. McFeely, A. Taleb-Ibrahimi, J.A. Yarmoff, and G. Holliger, *Phys. Rev. B* **38**, 6084 (1988).

<sup>26</sup>D.J. Lockwood, Z.H. Lu, and J.-M. Baribeau, *Phys. Rev. Lett.* **76**, 539 (1996).

<sup>27</sup>A. Pasquarello, M.S. Hybertsen, and R. Car, *Appl. Surf. Sci.* **104/105**, 317 (1996); A. Pasquarello, M.S. Hybertsen, and R. Car, *Appl. Phys. Lett.* **68**, 625 (1996).

<sup>28</sup>J.B. Neaton, D.A. Muller, and N.W. Ashcroft, *Phys. Rev. Lett.* **85**, 1298 (2000).

<sup>29</sup>Y. Tu and J. Tersoff, *Phys. Rev. Lett.* **84**, 4393 (2000).

<sup>30</sup>K.-O. Ng and D. Vanderbilt, *Phys. Rev. B* **59**, 10 132 (1999).

<sup>31</sup>H. Kageshima and K. Shiraishi, *Phys. Rev. Lett.* **81**, 5936 (1998).

<sup>32</sup>F. Herman and I.P. Batra, in *The Physics of SiO<sub>2</sub> and Its Interfaces*, edited by S.T. Pantelides (Pergamon, Oxford, 1978).

<sup>33</sup>N. Tit and M.W.C. Dharma-wardana, *Phys. Lett. A* **254**, 233 (1999).

<sup>34</sup>N. Tit and M.W.C. Dharma-wardana, *J. Appl. Phys.* **86**, 1 (1999).

<sup>35</sup>M. Tran, N. Tit, and M.W.C. Dharma-wardana, *Appl. Phys. Lett.* **75**, 4136 (1999).

<sup>36</sup>G. Kresse and J. Furthmüller, computer code VASP 4.4 (Vienna University of Technology, Vienna, 1997) [Improved and updated Unix version of the original copyrighted VASP/VAMP code, which was published by G. Kresse and J. Furthmüller, *Comput. Mater. Sci.* **6**, 15 (1996)].

<sup>37</sup>G. Kresse and D. Joubert, *Phys. Rev. B* **59**, 1758 (1999).

<sup>38</sup>P. Hohenberg and W. Kohn, *Phys. Rev.* **B136**, B864 (1964).

<sup>39</sup>W. Kohn and L.J. Sham, *Phys. Rev.* **A140**, A1133 (1965).

- <sup>40</sup>M.C. Payne, M.P. Teter, D.C. Allan, T.A. Arias, and J.D. Joannopoulos, *Rev. Mod. Phys.* **64**, 1045 (1992).
- <sup>41</sup>P.E. Blöchl, *Phys. Rev. B* **50**, 17 953 (1994).
- <sup>42</sup>D. J. Singh, *Planewaves, Pseudopotentials and the LAPW Method* (Kluwer Academic, Norwell, 1994).
- <sup>43</sup>B. Adolph, J. Furthmüller, and F. Bechstedt, *Phys. Rev. B* **63**, 125108 (2001).
- <sup>44</sup>P. Y. Yu and M. Cardona, *Fundamentals of Semiconductors* (Springer, New-York, 1996); G. Baym, *Lectures on Quantum Mechanics* (Addison-Wesley, Reading, MA, 1993); L. Ley, in *The Physics of Hydrogenated Amorphous Silicon II*, Vol. 56 of Topics in Applied Physics, edited by J.D. Joannopoulos and G. Lucovsky (Springer-Verlag, Berlin, 1984).
- <sup>45</sup>P.E. Blöchl, *Phys. Rev. B* **49**, 16 223 (1994).
- <sup>46</sup>E.K. Chang, M. Rohlfing, and S.G. Louie, *Phys. Rev. Lett.* **85**, 2613 (2000); S. Albrecht, L. Reining, R. Del Sole, and G. Onida, *ibid.* **80**, 4510 (1998).
- <sup>47</sup>M. Zacharias, J. Heitmann, and U. Gösele, *MRS Bulletin* **26**, 975 (2001).
- <sup>48</sup>J. Furthmüller (private communication).